Vol. 47, No. 4 (2025) 705-717, DOI: 10.24874/ti.1979.07.25.09

Tribology in Industry

www.tribology.rs

RESEARCH

# Design of Triaxial Impact Wear Tester: Finite Element Simulation for Performance Analysis of AA6061-T6 Alloy

Muhammed Raşit Karakoca[a,b,*], Ahmet Emrah Erdoğdu[a]

[a]*Department of Mechanical Engineering, Engineering Faculty, Karabuk University, Karabuk, Turkey,*
[b]*TAI, Turkish Aerospace Industries, Ankara, Turkey.*

Keywords:

*Impact wear*
*Finite element method*
*AA6061-T6*
*Shear stress*
*Shear strain*

* Corresponding author:

*Muhammed Raşit Karakoca*
*E-mail: karakoca22@itu.edu.tr*

*Received: 8 July 2025*
*Revised: 19 August 2025*
*Accepted: 25 September 2025*

A B S T R A C T

*Wear is a critical mechanism that directly affects the service life of engineering materials and can lead to premature system failure. To prevent wear-related losses, particularly encountered in manufacturing processes, test systems capable of simulating realistic laboratory conditions are needed. In this study, a three-dimensional wear tester was developed that can simultaneously evaluate impact effects with abrasive sliding. The system was designed to apply impact forces using a vibration motor and a spring-supported structure placed under the sample. CAD modeling was performed with SolidWorks software, and finite element analyses were performed using the ANSYS Explicit Dynamics module. Simulations were performed on AA6061-T6 alloy at speeds of 0.25, 0.50, and 1.00 m/s and loads of 10 N, 20 N and 40 N at a constant wear distance of 10 mm. The findings showed that wear depth, maximum shear stress, and elastic deformation values increased significantly with increasing load. A 50% load increase at a speed of 0.5 m/s increased wear depth by 39.8%. However, increasing speed under constant load limited these effects. It is anticipated that the developed system will contribute to the understanding of wear mechanisms and will be an important tool for evaluating material behavior under multiaxial loading.*



## 1. INTRODUCTION

Wear is one of the most critical factors influencing the service life of mechanical components, resulting from various mechanisms such as friction, fatigue, and chemical interactions. In numerous engineering applications, including automotive parts, aircraft engine turbine blades, mining equipment, and armored vehicle components, wear significantly impacts both system performance and structural integrity. Controlling wear is therefore of paramount importance in industrial settings, not only to enhance operational efficiency but also to minimize maintenance costs. Among the different types of wear, impact wear poses a particularly severe challenge in machinery operating under high-impact loading conditions [1–3].

Luo et al., to investigate the impact wear resistance of valve surfaces operating under high-temperature conditions, CrN coatings were applied to NCF3015, a nickel-based alloy, using plasma alloying technology. Impact wear tests were conducted using a custom-designed valve-seat impact testing apparatus. The results revealed that the surface hardness of the valves increased by approximately 2.4 times due to the applied coating, and the wear volume was significantly reduced—by approximately 63.7% to 74.6%—demonstrating a substantial improvement in wear resistance [4]. Mou et al. investigated the impact wear mechanism of titanium alloy (TC4) and stainless steel (9Cr18) substrates by applying diamond-like carbon (DLC) films and conducting tests using a newly designed impact wear testing device. The thickness of the DLC coatings were set at 1.1 μm and 7.9 μm. A comparative analysis of the coated specimens revealed a nano-hardness difference of approximately 19–20%, with the highest nano-hardness observed in the TC4 titanium alloy coated with a 1.1 μm DLC film. To quantify wear resistance, volumetric material loss was measured. The lowest wear volume was recorded in the specimen with the highest nano-hardness—namely, the titanium alloy with the 1.1 μm DLC coating—which exhibited approximately 64% less wear compared to its counterpart coated with the thicker 7.9 μm DLC layer [5]. Daniel et al. investigated the impact wear performance of Co-based coatings applied via high-velocity oxy-fuel (HVOF) spraying onto high-speed tool steel (DIN 1.2376) using a previously developed impact testing apparatus. Two coatings—CoCrW and CoCrAlYTaCSi—were applied with identical thicknesses of 400 μm. Wear behavior was evaluated under impact loads of 200 N, 400 N, and 600 N across a range of 1 to 100,000 impact cycles. While both coatings exhibited high durability with minimal wear under lower loads, the CoCrW-coated specimens demonstrated superior wear resistance under higher impact loads. Specifically, at 600 N and after 100,000 impacts, the CoCrW coating showed approximately 2.3 times less material loss compared to the CoCrAlYTaCSi coating [6]. Wang et al. investigated the wear performance of 2Cr13 martensitic stainless steel under low-stress multiple impact conditions using a flat-on-flat impact testing apparatus. At lower impact counts—up to 10,000 cycles—only the surface of the material was affected, exhibiting localized work hardening. However, as the number of impacts increased, subsurface deformation extended to a depth of approximately 140 μm at 80,000 cycles. This progressive hardening was found to increase the risk of surface embrittlement. Moreover, a comparison between 10,000 and 80,000 impact cycles revealed a dramatic increase in mass loss, with the total weight loss rising by approximately 1100%, underscoring the severity of cumulative impact damage under extended loading [7]. In another study, Gümüşlü et al. examined the influence of temperature on the impact-sliding wear behavior of 316L austenitic stainless steel. Utilizing a previously reported impact-sliding wear testing device with modifications, they conducted experiments at two distinct temperatures: room temperature and 180 °C. When comparing the impact wear region to the sliding wear region, they found that impact loading resulted in significantly greater material loss. Furthermore, increasing the test temperature from room temperature to 180 °C led to a dramatic change in wear behavior: the wear rate in the impact zone increased by approximately 110%, whereas the wear rate in the sliding zone decreased by about 65%. These findings highlight the contrasting effects of elevated temperature on different wear mechanisms within the same material [8].

In engineering design, enhancing the mechanical performance and wear resistance of materials is of critical importance for developing durable and long-lasting components. In this context, Finite Element Analysis (FEA), which has gained widespread application in recent years, serves as a powerful tool for predicting material behavior under mechanical loading and wear conditions. FEA not only accelerates the design process but also provides a scientific foundation for optimization studies, enabling detailed investigation of material responses under complex loading scenarios [9,10].

Conventional wear testing devices reported in the literature typically operate under static or low dynamic loading conditions and are therefore unable to realistically simulate impact-induced wear mechanisms. Addressing this limitation, the present study introduces an innovative testing system capable of

simultaneously modeling both impact and abrasive wear, with the added advantage of three-dimensional motion capability. The proposed design distinguishes itself not only in terms of loading but also through its multi-axial motion configuration, setting it apart from conventional systems. Finite Element Analysis (FEA) was performed on AA6061-T6 alloy under various speed and force combinations to evaluate wear behavior. The findings are expected to contribute valuable insights to material selection, surface engineering, and mechanical design processes.

## 2. MATERIALS AND METHODS

### 2.1 Experimental setup

In the initial phase of the study, a vibration-assisted impact-sliding wear testing device was designed. The apparatus was developed in accordance with ASTM G133-05 standards using the three-dimensional solid modeling interface of SOLIDWORKS software (Fig. 1). It was engineered to allow precise control of both the applied normal load and sliding speed, enabling flexible and accurate test configurations.

To facilitate the generation of impact forces, a vibration motor was integrated into the design. Linear motion of the movable specimen holder beneath a stationary ball enables the simulation of abrasive wear through controlled reciprocating contact. In addition, the vibration motor induces oscillatory motion via a spring system, applying periodic impact forces to the test table and thereby activating the impact wear mechanism.

As a result, the system was rendered fully functional for the simultaneous and synchronized simulation of both abrasive and impact wear mechanisms. The impact force is transmitted from beneath the fixture directly to the specimen, allowing for realistic and controlled modeling of complex wear conditions within a laboratory environment.

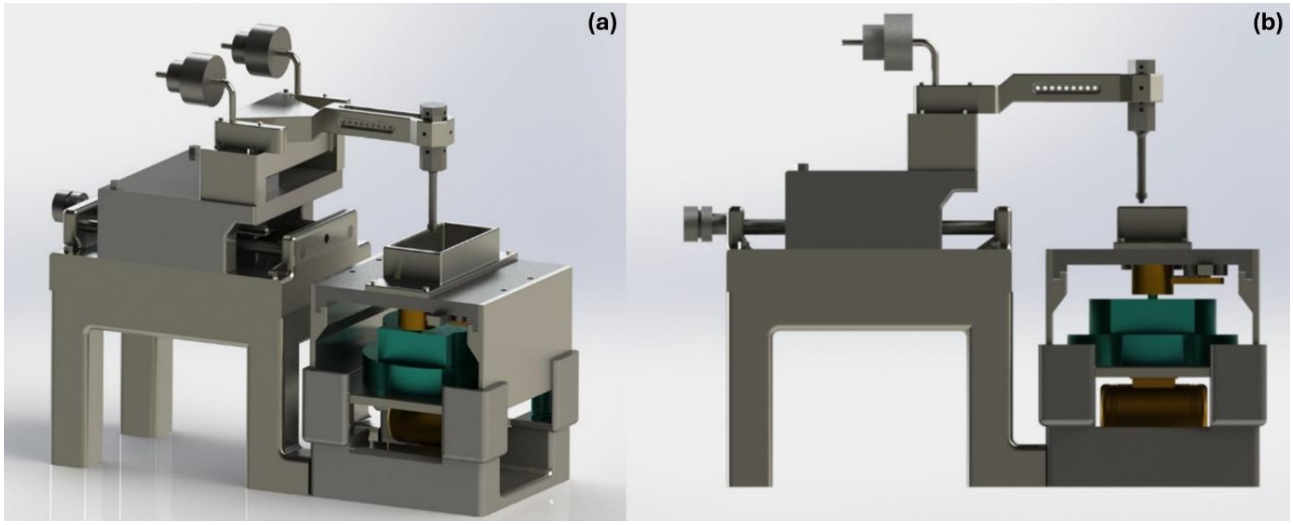


**Fig. 1**. Model of the vibration-assisted impact-sliding wear test device; (a) isometric view, (b) right-hand sectional view.

The rotational motion generated by the servo motor is mechanically transmitted to an eccentric shaft, where it is converted into linear motion along a single axis (Fig. 2). This mechanism enables directional control of movement along a specific coordinate axis, resulting in a precise and repeatable linear displacement. As the linear motion table operates, the mounted specimen comes into contact with a stationary abrasive surface, initiating the wear process under controlled and reproducible conditions.

**Fig. 2.** Eccentric shaft and linear motion table.

To generate impact forces within the system, a vibration motor was employed. Operating at a defined amplitude, this motor is capable of producing multidirectional oscillatory motion. The vibration motor is mounted at the lower section of the test assembly, and a spring mechanism is integrated at each of the four corners of the platform to which the motor is attached (Fig. 3). Upon activation, the system positioned atop the springs undergoes multidirectional oscillation. However, to constrain the oscillatory motion exclusively to the Z-axis, directional guides have been incorporated into the system to restrict movement in undesired directions.

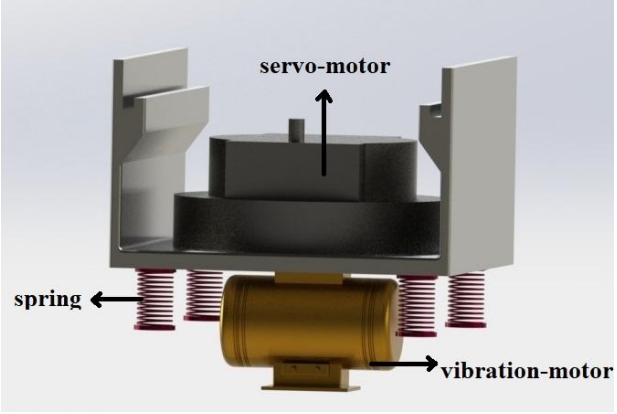


**Fig. 3.** Positions of the vibration motor and springs.

The oscillatory motion enables the periodic application of impact forces to the contact interface between the stationary abrasive tip and the specimen. This configuration facilitates the simultaneous simulation of both sliding and impact wear conditions.

The selection of the vibration motor was guided by insights from relevant literature, which informed the amplitude requirements of the system. In particular, it has been determined that the vibration motor in contact with the fixture body must operate with a vibration amplitude below 0.1 mm to ensure proper simulation, accuracy and mechanical stability [11].

The dynamic behavior of the vibration system was modeled using the following equations:

$$F_M: A_{pp} \times m_t \; x \; \left(\frac{n}{1000}\right)^2 \times 0.56 \; [N] \qquad (1)$$

$$M: e \times m_t \; [Nmm] \qquad (2)$$

$$e: A_{pp}/2 \; [mm] \qquad (3)$$

In these equations:
$F_M: Centrifugal\ force\ [N]$
$M: Static\ moment\ [Nmm]$
$A_{pp}: Vibration\ amplitude\ [mm]$
$m_t: System\ total\ mass\ with\ motor\ [kg]$
$e: Eccentricity\ [mm]$
$n: Motor\ speed\ [rpm]$

In this configuration, the total weight of the system—including the vibration motor—was calculated to be approximately 20 N. When operating at a vibration amplitude of 0.1 mm, the system generates a static moment of approximately 1 N·mm. This static moment corresponds to a repeated impact force of roughly 20 N applied at the contact interface between the specimen and the abrasive tip.

## 2.2 Analysis setup

ANSYS software enables theoretical modeling of complex engineering systems and facilitates their analysis under a wide range of physical conditions [12,13]. In this study, the Explicit Dynamics module was selected as the analysis method, given that the test system was designed to apply impact forces simultaneously with linear sliding motion. This module was deemed the most appropriate for accurately representing the physical behavior of the system, due to its ability to simulate short-duration, high-speed contact and impact events with high precision [14,15].

To develop a numerical model that closely reflects real-world behavior, fundamental mechanical properties such as Young's modulus, mass density, Poisson's ratio, shear modulus, and yield strength—along with other relevant material parameters—were defined in the ANSYS software in accordance with international standards. Accurate specification of these parameters enhances the reliability of numerical analysis and enables meaningful comparison with experimental results.

In the present study, the specimen was mounted on a linearly moving table, while the abrasive tip was positioned in a fixed orientation against the specimen surface. The system was designed to allow the application of various load levels to accommodate different experimental requirements. The linear motion of the table was driven by a servo motor connected to an eccentric shaft.

During testing, the servo motor provided continuous sliding motion, while the vibration motor operated synchronously. The oscillatory motion generated by the vibration motor was transmitted to the table through an integrated spring mechanism. This resulted in the periodic application of impact forces at the contact interface between the specimen and the abrasive tip, allowing the system to simultaneously impose both linear sliding and impact loading conditions.

To investigate the structural effects of this hybrid loading scenario, the system was adapted for finite element analysis (FEA), and simulations were conducted using the "Explicit Dynamics" module in ANSYS Workbench 19.2. The material used for the test specimen in the simulations was AA6061-T6 aluminum alloy.

The Explicit Dynamics module includes a range of material models capable of capturing different deformation regimes. In this study, the Johnson–Cook elasto-plastic material model was selected for its ability to realistically represent the physical behavior of the alloy. This model expresses stress as a function of both plastic strain and strain rate, making it particularly well-suited for simulating mechanical responses under high deformation rates [16,17]. In this study, the Johnson–Cook model was selected to enhance the accuracy of the simulations and to best replicate the experimental conditions.

### 2.3 Three- Dimensional model

The test device developed in this study was specifically designed to accommodate spherical abrasive elements. Tungsten balls with a diameter of 6 mm were selected as the abrasive medium, owing to the high hardness and wear resistance of tungsten, which ensures stable abrasive behavior under repeated loading conditions.

The device was configured to perform wear tests on rectangular prism specimens with dimensions of $3 \times 5 \times 12\ mm^3$. In both experimental and numerical analyses, AA6061-T6 aluminum alloy was used as the specimen material. This alloy is well known for its favorable wear resistance, excellent formability, and suitability for machining operations, making it an ideal candidate for tribological studies.

AA6061-T6 alloy exhibits high mechanical strength and a stable microstructure following solution heat treatment. Additionally, its excellent weldability and surface machinability make it a widely preferred material in various engineering applications [18,19]. The chemical composition and mechanical properties of the AA6061-T6 alloy are presented in Table 1 and Table 2, respectivel.

**Table 1.** Chemical composition of AA6061-T6 alloy [20].

| Elements | Mg | Si | Fe | Cu | Cr | Zn | Ti | Mn | Al |
|---|---|---|---|---|---|---|---|---|---|
| Wt% | 1.2 | 0.81 | 0.7 | 0.4 | 0.35 | 0.25 | 0.15 | 0.15 | Balance |

**Table 2.** Mechanical properties of AA6061-T6 alloy [20].

| Yield Strength (MPa) | Tensile Strenght (MPa) | Elongation (%) | Hardness (HV) |
|---|---|---|---|
| 225 | 282.4 | 17 | 107 |

### 2.4 Wear simulation parameters: coordinate, contact region, meshing

The wear simulations were conducted based on Archard's wear model law, which relates material removal to applied load, sliding distance, and material hardness, providing a theoretical framework for evaluating wear depth under varying conditions.

The coordinate axes used in the test system are illustrated in Fig. 4, and all analyses were conducted with respect to these axis orientations.

During testing, the table holding the specimen moves at a constant speed along the X-axis beneath a fixed abrasive ball. Simultaneously, oscillatory motion induced by the vibration motor generates periodic impact forces along the negative Z-axis through a spring mechanism. In addition, a constant adjustable normal load is applied along the Z-axis, exerting compressive force between the abrasive ball and the specimen.

In the simulations, contact regions were defined to realistically replicate experimental conditions. Accordingly, contact was modeled exclusively

between the specimen and the abrasive ball at their interface. As the material properties and interactions at this interface directly influence the accuracy of the simulation, careful definition of these parameters was essential. The contact between the specimen and the ball was modeled as a nonlinear interaction. The contact stiffness was set to the default "normal" value, with a stiffness factor of 0.1.

To prevent geometric penetration during iterative steps, the Augmented Lagrange method was employed in the contact algorithm. The Z-facing surface of the ball was aligned to be in contact with the surface of the specimen oriented in the negative Z direction (Fig. 4). Wear was assumed to develop primarily on the specimen surface, which has lower mechanical strength relative to the abrasive ball.

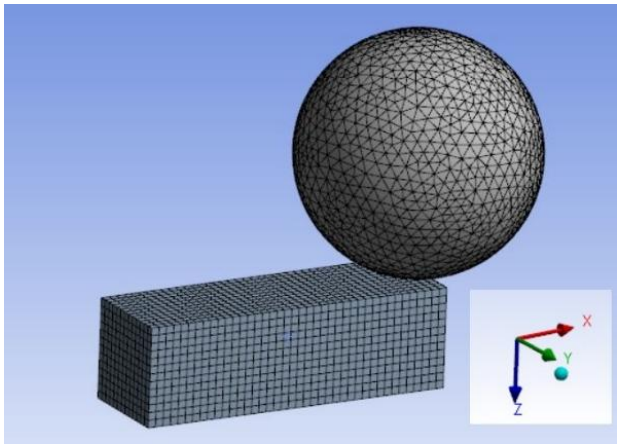


**Fig. 4.** Meshed model of the specimen and abrasive ball.

In finite element method (FEM) analyses, the primary purpose of meshing is to discretize the volume of geometrically complex components into smaller, solvable subdomains. As the mesh size decreases, the accuracy of the analysis improves; however, this also leads to a proportional increase in computational time. Therefore, it is essential to establish an optimal balance between mesh refinement and analysis efficiency [21,22]. The computational power of the hardware used plays a critical role in this context. To evaluate mesh quality, mesh sensitivity analyses were conducted, comparing the effects of different mesh sizes on both wear depth and computational time. These analyses were performed under fixed conditions: a sliding speed of 0.25 m/s, an applied load of 20 N, and a total wear distance of 10 mm. The mesh configurations and corresponding analysis results are presented in Table 3.

**Table 3.** Analysis time results corresponding to mesh sensitivity.

| Analysis ID | Element size (mm) | Wear Depth (mm) | Analysis Time (s) |
|---|---|---|---|
| 1 | 1 | -0.18221 | 1.6 |
| 2 | 0.5 | -0.14167 | 2.8 |
| 3 | 0.25 | -0.12965 | 4.6 |
| **4** | **0.1** | **-0.08904** | **7.6** |
| 5 | 0.05 | -0.08968 | 12.7 |

Based on the results of the sensitivity analyses and considering the available computational resources, an optimal mesh size of 0.1 mm was selected. The finite element model of the specimen and tungsten ball using this mesh resolution is illustrated in Fig. 4. All simulations were carried out on a workstation equipped with 32 GB of RAM, 6 GB of GPU memory, and an 8-core processor operating at 2.4 GHz. To reduce computation time, all processor cores were utilized for parallel processing.

The selected mesh configuration contains a defined number of nodes and elements, both of which directly influence the accuracy of the simulation results [23,24]. For the abrasive tungsten ball, the Hex Dominant meshing method was employed. Due to the spherical geometry of the ball, variations in element size were particularly evident in the polar regions (i.e., the top and bottom areas). The Hex Dominant approach was selected for its ability to generate a well-balanced and high-quality mesh across the entire geometry. The specimen, fabricated from AA6061-T6 alloy, has a rectangular prism shape and was meshed using four-node quadrilateral elements. The corresponding mesh structures are illustrated in Fig. 4.

### 2.5 Applied load, velocity and boundary conditions

In this study, the applied load and sliding velocity were defined as variable parameters, while the wear distance was held constant at 10 mm. Due to the system configuration, a constant impact force of 20 N is generated in the negative Z-axis direction by the vibration motor. In addition to this intrinsic force, external loads of 10 N and 20 N were applied to the test setup, resulting in total applied forces of 20 N, 30 N, and 40 N, respectively (Fig. 5).

These force conditions were defined as boundary conditions within the ANSYS Explicit Dynamics module and simulated as separate loading scenarios. All applied forces were modeled to act along the Z-axis direction.

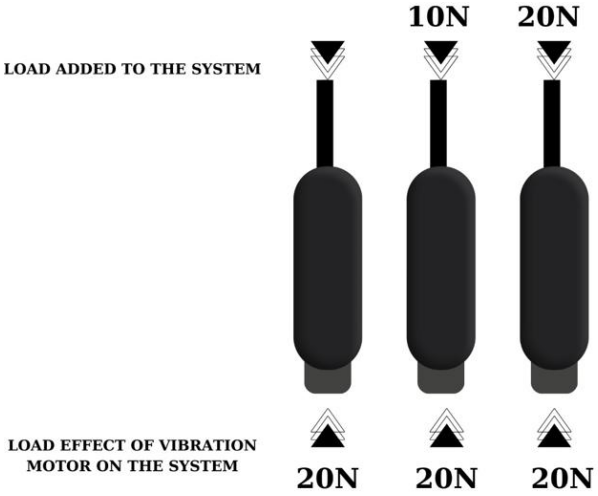


**Fig. 5.** Applied forces acting on the specimen.

In the test scenarios, the specimen moves linearly along the X-axis at a constant velocity defined by a servo motor. Based on experimental and numerical literature references, the sliding speeds used in the simulations were selected as 0.25 m/s, 0.5 m/s, and 1 m/s. These speed values were applied under a fixed wear distance of 10 mm, and system behavior was evaluated throughout the corresponding analysis durations.

For each speed value, the designated end time parameters and associated simulation durations are provided in detail in Table 4. This approach allows for a comprehensive assessment of the influence of load and velocity on the wear mechanism.

**Table 4.** Defined end time parameters and simulation durations for different velocity values.

| Analysis ID | Vx (m/s) | t (s) | Load (N) |
|---|---|---|---|
| 1 | 0,25 | 0,04 | 20 |
| 2 | 0,25 | 0,04 | 30 |
| 3 | 0,25 | 0,04 | 40 |
| 4 | 0,5 | 0,02 | 20 |
| 5 | 0,5 | 0,02 | 30 |
| 6 | 0,5 | 0,02 | 40 |
| 7 | 1 | 0,01 | 20 |
| 8 | 1 | 0,01 | 30 |
| 9 | 1 | 0,01 | 40 |

## 3. ANALYSIS RESULTS

Following the completion of the design of the vibration-assisted abrasive wear testing device, the mechanical behavior of the system was analyzed using the Finite Element Method (FEM). Numerical simulations were carried out using the Explicit Dynamics module within ANSYS Workbench, based on the defined boundary conditions.

In the analyses, AA6061-T6 aluminum alloy was selected as the specimen material, while a high-hardness tungsten ball was used as the abrasive element. The system was modeled to simulate the wear behavior caused by frictional contact between the specimen, moving at a constant velocity under predefined loads, and the abrasive ball.

Within the defined boundary conditions, three different sliding speeds—0.25 m/s, 0.50 m/s, and 1.00 m/s—were applied. In addition to the constant impact force generated by the vibration motor, supplementary external loads of 10 N and 20 N were introduced. For each simulation scenario, the target wear distance was fixed at 10 mm, and the corresponding end time values were calculated to configure the simulation parameters.

The simulation outputs included quantitative evaluations of, wear depths, maximum shear stress, and maximum shear strains. These results were comparatively analyzed across different speed and load combinations to assess their influence on the wear mechanism.

### 3.1 Wear depth

The maximum wear depth results obtained from the simulations are presented in Fig. 6. The simulations were performed under a fixed wear distance of 10 mm, with sliding speeds defined as 0.25 m/s, 0.50 m/s, and 1.00 m/s, and applied forces set at 20 N, 30 N, and 40 N. Under constant speed conditions, an increase in the applied force resulted in a corresponding increase in wear depth. At a sliding speed of 0.25 m/s, increasing the load by 50% (from 20 N to 30 N) led to a 7.53% increase in wear depth, while a further 33.33% increase in load (from 30 N to 40 N) resulted in a 27.37% rise.

At 0.50 m/s, the same force increments yielded increases of 39.80% and 12.41%, respectively. At 1.00 m/s, wear depths rose by 32.83% and 9.82% with the same load increases. Detailed numerical values are provided in Table 5.

These results demonstrate that wear depth increases proportionally with load but decreases as sliding speed increases under constant loading. This behavior can be attributed to the reduced effective contact time and contact area between the specimen and the abrasive surface at higher speeds. A smaller contact area limits the magnitude of frictional forces, thereby reducing the effective pressure applied and consequently the overall wear. The findings are consistent with wear trends reported in the literature [25–27].

The wear depth predictions are based on Archard's wear model law, which relates material loss to applied load, sliding distance, and material hardness, providing a theoretical foundation for the observed trends.

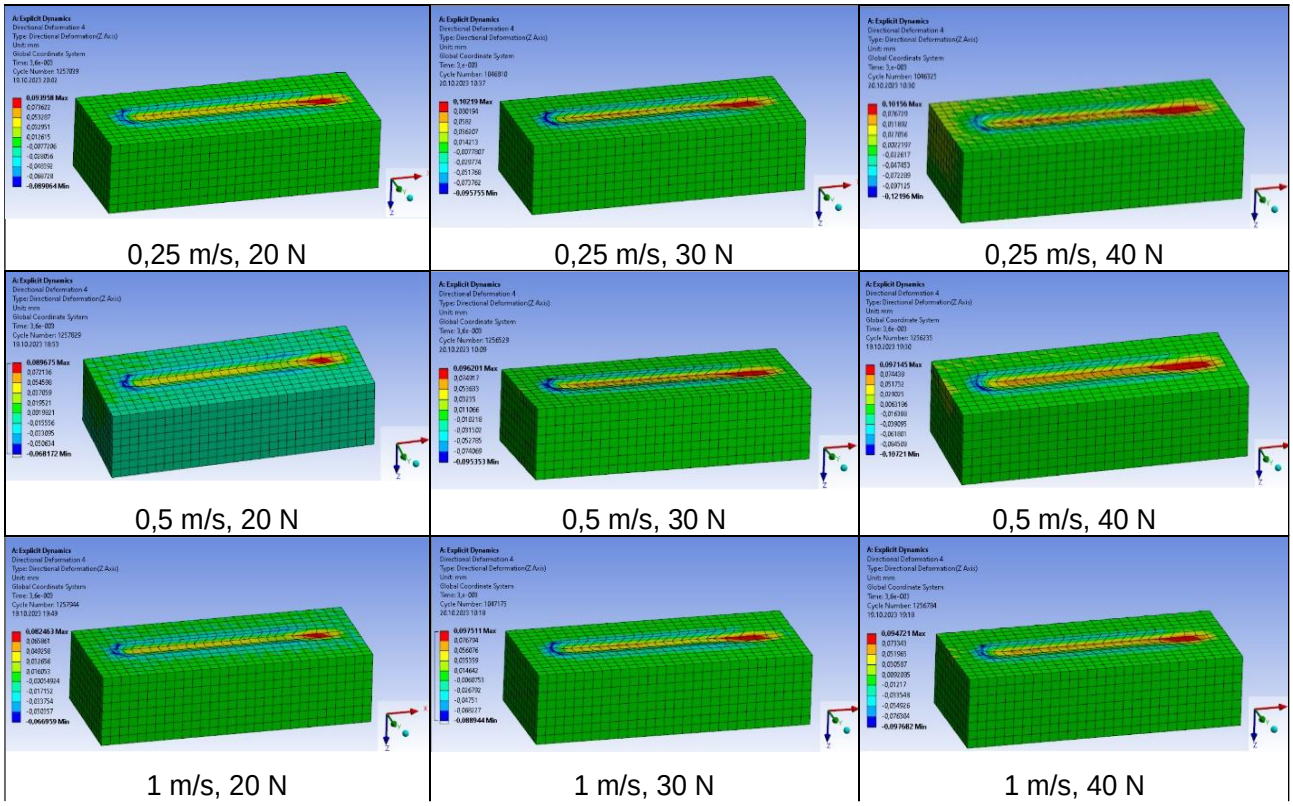


**Fig. 6.** Maximum wear depth distributions.

**Table 5.** Wear depth analysis results under varying sliding speed and load conditions.

| Sliding Speed (m/s) | Load (N) | Wear Depth (mm) |
|---|---|---|
| 0,25 | 20 | -0,08904 |
| | 30 | -0,09575 |
| | 40 | -0,12196 |
| 0,5 | 20 | -0,068172 |
| | 30 | -0,095353 |
| | 40 | -0,10721 |
| 1 | 20 | -0,066959 |
| | 30 | -0,088944 |
| | 40 | -0,097682 |

### 3.2 Shear stress

The maximum shear stress values obtained from the simulations are presented in Fig. 7. Shear stress arises when external forces acting on structural components are not aligned with internal forces, and it plays a critical role in evaluating the structural integrity of systems subjected to contact and frictional effects.

In this study, simulations were performed under a fixed wear distance of 10 mm, with sliding speeds set at 0.25 m/s, 0.50 m/s, and 1.00 m/s, and applied loads defined as 20 N, 30 N, and 40 N. The key findings can be summarized as follows: at a sliding speed of 0.25 m/s, increasing the load by 50% (from 20 N to 30 N) resulted in a 3.02% increase in maximum shear stress. A further 33.33% increase in load (from 30 N to 40 N) produced a 2.12% rise. At 0.50 m/s, these load increments led to increases of 2.60% and 2.48%, respectively. At 1.00 m/s, the maximum shear stress increased by 3.05% and 3.20% for the same respective load increases. Detailed numerical data are provided in Table 6.

Based on these findings, the following general trends were observed: under constant sliding speed conditions, an increase in the applied load leads to a corresponding rise in maximum shear stress. This is attributed to the intensified tendency for plastic deformation in the contact region as a result of higher loading. Conversely, under constant load conditions, increasing the sliding speed tends to cause relatively smaller increases—or in some cases, reductions—in shear stress. This behavior is primarily associated with the shortened contact duration and reduced instantaneous contact area at higher speeds, which in turn diminishes the transmission of stress. Notably, similar effects are reflected in the wear mechanisms, highlighting the critical influence of sliding speed on both mechanical response and material degradation. [28,29].

In conclusion, the stress-enhancing effect of increasing load on the material was clearly confirmed, while the stress-limiting influence of higher sliding speeds was particularly evident at moderate and high velocity levels. These relationships represent important findings that validate both the structural design of the wear testing system and the accuracy of the defined boundary conditions.

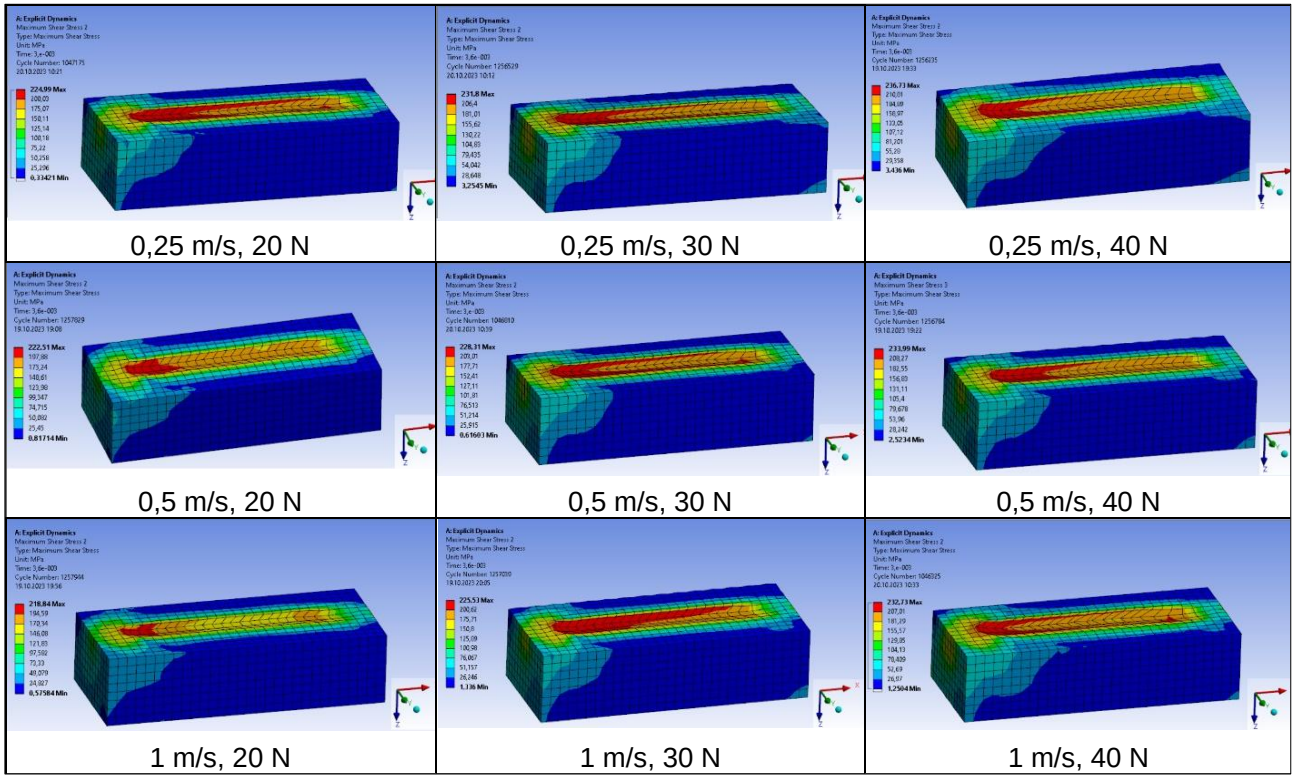


**Fig. 7.** Maximum shear stress values obtained from the simulations.

**Table 6.** Shear stress analysis results under varying sliding speed and load conditions.

| Sliding Speed (m/s) | Load (N) | Shear Stress (MPa) |
|---|---|---|
| 0,25 | 20 | 224,99 |
| | 30 | 231,80 |
| | 40 | 236,73 |
| 0,5 | 20 | 222,51 |
| | 30 | 228,31 |
| | 40 | 233,99 |
| 1 | 20 | 218,84 |
| | 30 | 225,53 |
| | 40 | 232,73 |

### 3.3 Shear strain

The maximum elastic shear strain values obtained from the simulations are presented in Fig. 8. Strain is defined as the amount of deformation per unit volume resulting from externally applied loads, and elastic strain specifically represents the material's response prior to the onset of permanent deformation.

The simulation parameters were set under a constant wear distance of 10 mm, with sliding speeds of 0.25 m/s, 0.50 m/s, and 1.00 m/s, and applied loads of 20 N, 30 N, and 40 N, respectively. According to the obtained results: at a sliding speed of 0.25 m/s, a 50% increase in load (from 20 N to 30 N) led to a 45.6% increase in maximum elastic shear strain, while a 33.33% increase in load (from 30 N to 40 N) resulted in a 39.0% increase. At 0.50 m/s, the same load increments yielded increases of 63.0% and 23.0%, respectively. At 1.00 m/s, elastic shear strain increased by 48.5% and 41.7% for the corresponding load increases. Detailed numerical results are presented in Table 7.

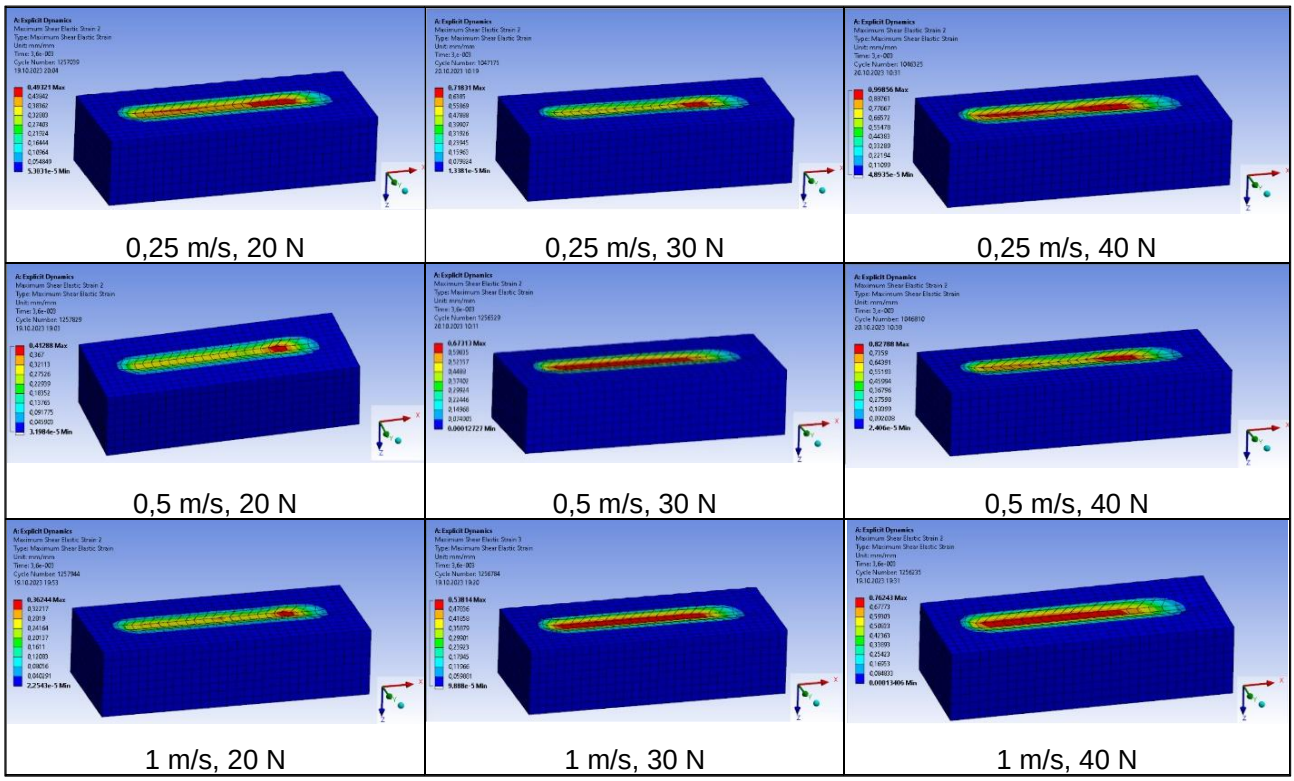


**Fig. 8.** Maximum elastic shear strain values obtained from the simulations.

**Table 7**. Elastic shear strain analysis results under varying sliding speed and load conditions.

| Sliding Speed (m/s) | Load (N) | Elastic Shear Strain (mm/mm) |
|---|---|---|
| 0,25 | 20 | 0,49321 |
| | 30 | 0,71831 |
| | 40 | 0,99856 |
| 0,5 | 20 | 0,41288 |
| | 30 | 0,67313 |
| | 40 | 0,82788 |
| 1 | 20 | 0,36244 |
| | 30 | 0,53814 |
| | 40 | 0,76243 |

These findings indicate that, under constant speed conditions, increasing the applied load significantly enhances the material's elastic deformation capacity, leading to notable increases in maximum elastic strain. Conversely, under constant load conditions, increasing the sliding speed reduces the effective contact time between the specimen and the abrasive element, which in turn lowers the level of elastic deformation. This effect can be attributed to the shorter energy transfer duration at the contact interface and the restricted propagation of stress within the deformation zone [30–32].

In conclusion, the direct enhancing effect of increased load on elastic strain was observed across all velocity scenarios. However, at higher sliding speeds, this increase was comparatively more limited, highlighting the moderating influence of velocity on both wear and deformation behavior.

## 4. CONCLUSIONS

In engineering applications, predicting the service life, strength characteristics, and potential early failure mechanisms of materials is a critical factor in terms of both performance and cost. This study focuses on wear mechanisms, one of the primary causes of material degradation during manufacturing, which can lead to significant reductions in component lifespan and production efficiency.

The main objective of the study is the development of a vibration-assisted impact-abrasive wear testing device, along with the finite element modeling (FEA) of this system, to analyze its structural response under various loading and velocity conditions.

To this end, the vibration-assisted impact wear tester was designed in compliance with ASTM G133-05 using SolidWorks CAD software. The system dimensions were tailored for practical applicability. The vibration motor, which introduces the impact loading capability to the device, was selected to operate at an amplitude of 0.1 mm and deliver an approximate force of 20 N. For the numerical simulations, AA6061-T6 aluminum alloy was selected as the specimen material, while high-hardness tungsten balls were used as the abrasive elements. Finite element analyses were conducted using the Explicit Dynamics module in ANSYS Workbench 19.2. Boundary conditions were defined for a constant wear distance of 10 mm under sliding velocities of 0.25 m/s, 0.50 m/s, and 1.00 m/s, with additional external loads of 10 N and 20 N.
The key findings of the simulations are summarized as follows:

- Wear depth increased with applied load across all speeds. At 0.25 m/s, a 50% increase in force (from 20 N to 30 N) led to a 7.53% rise in wear depth, while a 33.33% increase (from 30 N to 40 N) resulted in a 27.37% rise. At 0.50 m/s, the same increments caused increases of 39.8% and 12.41%, respectively. At 1.00 m/s, the wear depth increased by 32.83% and 9.82%.
- Under the same conditions, maximum shear stresses were also evaluated. At 0.25 m/s, load increases of 50% and 33.33% led to stress increases of 3.02% and 2.12%, respectively. For 0.50 m/s, the same load increments produced increases of 2.60% and 2.48%. At 1.00 m/s, shear stress rose by 3.05% and 3.20% with the corresponding load increases.

- Maximum elastic shear strain values were also analyzed. At 0.25 m/s, a 50% increase in load caused a 45.6% rise in strain, while a 33.33% increase yielded a 39.0% rise. At 0.50 m/s, the respective increases were 63.0% and 23.0%, and at 1.00 m/s, they were 48.5% and 41.7%.

The results highlight the system's sensitivity to load and speed parameters. At constant sliding speed, increasing the applied force led to significant rises in wear depth, stress, and elastic strain. However, under constant load, increasing the sliding speed had a mitigating or diminishing effect on these responses. This behavior is attributed to the reduced effective contact time and smaller contact area at higher speeds.

Overall, the outcomes of this study provide valuable insights into the structural behavior and modeling accuracy of vibration-assisted hybrid wear systems. These findings serve as a meaningful reference for the design and simulation of similar mechanical systems.

## Acknowledgement

This study was carried out within the scope of the LIFT UP++ Industry-Oriented Doctoral Research Program, supported by Turkish Aerospace Industries Inc. (TUSAŞ).

## REFERENCES

[1] B. Swain, S. Bhuyan, R. Behera, S. Sanjeeb Mohapatra, and A. Behera, "Wear: A Serious Problem in Industry," in *IntechOpen eBooks,* 2020. doi: 10.5772/intechopen.94211.

[2] Y. Chen, W. Gong, and R. Kang, "Review and propositions for the sliding/impact wear behavior in a contact interface," *Chinese Journal of Aeronautics*, vol. 33, no. 2, pp. 391–406, Jun. 2018, doi: 10.1016/j.cja.2018.06.004.

[3] A. Orak, S. Korkmaz, and M. H. Cetin, "Investigation of wear and corrosion resistance of WC-coated Pearlitic railway steel in dry and wet conditions," *International Journal of Refractory Metals and Hard Materials*, vol. 130, p. 107163, Mar. 2025, doi: 10.1016/j.ijrmhm.2025.107163.

[4] C. Luo, Y. Yao, D. Wei, M. Lin, P. Zhang, and S. Qu, "Impact Wear Behavior of the Valve Cone Surface after Plasma Alloying Treatment," *Applied Sciences,* vol. 14, no. 11, p. 4811, Jun. 2024, doi: 10.3390/app14114811.

[5] C. Mou, Z. Liu, G. Zhu, G. Zhang, and X. Cao, "Study on impact wear and damage mechanisms of DLC films on TC4 and 9Cr18 alloys," *Diamond and Related Materials,* vol. 148, p. 111390, Jul. 2024, doi: 10.1016/j.diamond.2024.111390.

[6] J. Daniel, Š. Houdková, J. Dulíškovič, and J. Grossman, "Impact wear of the Co-based HVOF-sprayed coatings," *Tribology International,* vol. 187, p. 108755, Jul. 2023, doi: 10.1016/j.triboint.2023.108755.

[7] S. Wang, Q. Cui, J. Zou, and Z. Zhang, "Impact wear mechanism of 2Cr13 steel under small stress multi-impact conditions," *Wear*, vol. 462–463, p. 203492, Sep. 2020, doi: 10.1016/j.wear.2020.203492.

[8] T. Gumuslu, M. Kaba, E. Atar, and H. Cimenoglu, "Effect of testing temperature on the impact-sliding wear behaviour of a 316L austenitic stainless steel," in *Materials Today: Proceedings*, vol. 81, pp. 81–86, Jan. 2023, doi: 10.1016/j.matpr.2023.04.116.

[9] T. Lu, X. Wu, Y. Wang, P. Shang, and Z. Zhu, "Finite element analysis and experimental study on fretting wear of different contact surfaces of fir-tree joint," *Tribology International,* vol. 207, p. 110631, Mar. 2025, doi: 10.1016/j.triboint.2025.110631.

[10] A. Haider, "Efficiency enhancement techniques in finite element analysis: navigating complexity for agile design exploration," *Aircraft Engineering and Aerospace Technology*, vol. 96, no. 5, pp. 662–668, May 2024,, doi: 10.1108/AEAT-02-2024-0053.

[11] K. Elleuch and S. Fouvry, "Wear analysis of A357 aluminium alloy under fretting," *Wear*, vol. 253, no. 5–6, pp. 662–672, Sep. 2002, doi: 10.1016/S0043-1648(02)00116-3.

[12] P. Põdra and S. Andersson, "Simulating sliding wear with finite element method," *Tribology International*, vol. 32, no. 2, pp. 71–81, Feb. 1999, doi: 10.1016/S0301-679X(99)00012-2.

[13] S. K. Chimakurthi, S. Reuss, M. Tooley, and S. Scampoli, "ANSYS Workbench System Coupling: a state-of-the-art computational framework for analyzing multiphysics problems," *Engineering With Computers,* vol. 34, no. 2, pp. 385–411, Nov. 2017, doi: 10.1007/s00366-017-0548-4.

[14] M. Yan and W. Tao, "Finite Element Analysis of Cylinder Piston Impact Based on ANSYS/LS-DYNA," *Proceedings of the 1st International Conference on Mechanical Engineering and Material Science*, Jan. 2012, doi: 10.2991/mems.2012.66.

[15] S. Dumitru, A. Constantin, C. Copilusi, and N. Dumitru, "Impact dynamics analysis of mobile mechanical systems," *Mathematics*, vol. 9, no. 15, Jul. 2021, doi: 10.3390/math9151776.

[16] Q. Li, "Computational modeling of dynamic mechanical properties of pure polycrystalline magnesium under high loading strain rates," in *EPJ Web of Conferences*, vol. 94, p. 01019, Jan. 2015, doi: 10.1051/epjconf/20159401019.

[17] B. Revil-Baudard, G. Kleiser, N. Chandola, and O. Cazacu, "Plastic deformation of metallic materials during dynamic events," in *Journal of Physics: Conference Series*, vol. 1063, p. 012054, Jul. 2018, doi: 10.1088/1742-6596/1063/1/012054.

[18] B. Bagheri, M. Abbasi, and A. Abdollahzadeh, "Microstructure and mechanical characteristics of AA6061-T6 joints produced by friction stir welding, friction stir vibration welding and tungsten inert gas welding: A comparative study," *International Journal of Minerals, Metallurgy and Materials*, vol. 28, no. 3, pp. 450–461, Mar. 2021, doi: 10.1007/s12613-020-2085-1.

[19] B. T. Ogunsemi, T. E. Abioye, T. I. Ogedengbe, and H. Zuhailawati, "A review of various improvement strategies for joint quality of AA 6061-T6 friction stir weldments," *Journal of Materials Research and Technology,* vol. 11, pp. 1061–1089, Jan. 2021, doi: 10.1016/j.jmrt.2021.01.070.

[20] P. Rajalingam, S. Rajakumar, S. Kavitha, and T. Sonar, "Ultrasonic spot-welding of AA 6061-T6 aluminium alloy: Optimization of process parameters, microstructural characteristics and mechanical properties of spot joints," *International Journal of Lightweight Materials and Manufacture,* vol. 7, no. 1, pp. 25–36, Jul. *2023*, doi: 10.1016/j.ijlmm.2023.07.002.

[21] C. Curreli, F. Di Puccio, and L. Mattei, "Application of the finite element submodeling technique in a single point contact and wear problem," *International Journal for Numerical Methods in Engineering,* vol. 116, no. 10–11, pp. 708–722, Aug. 2018, doi: 10.1002/nme.5940.

[22] Z. Bin, D. Yannan, O. Weiping, T. Xiaoying, and X. Xiaolong, "Research on Finite Element Optimal Analysis Method," in *IOP Conference Series: Earth and Environmental Science*, vol. 310, no. 4, p. 042021, Aug. 2019. doi: 10.1088/1755-1315/310/4/042021.

[23] N. H. Kim *et al.*, "Finite element analysis and experiments of metal/metal wear in oscillatory contacts," *Wear*, vol. 258, no. 11–12, pp. 1787–1793, Jan. 2005, doi: 10.1016/j.wear.2004.12.014.

[24] H. Benabdallah and D. Olender, "Finite element simulation of the wear of polyoxymethylene in pin-on-disc configuration," *Wear*, vol. 261, no. 11–12, pp. 1213–1224, May 2006, doi: 10.1016/j.wear.2006.03.040.

[25] C. Wu, Z. Jiang, W. Fan, and L. Chen, "Finite element analysis of multi-wire saw silicon rods with consolidated abrasive diamonds," *International Journal of Advanced Manufacturing Technology*, vol. 90, no. 1–4, pp. 241–248, Aug. 2016, doi: 10.1007/s00170-016-9321-x.

[26] A. M. Al-Qutub, I. M. Allam, and M. A. Abdul Samad, "Wear and friction of Al-Al2O3 composites at various sliding speeds," *Journal of Materials Science,* vol. 43, no. 17, pp. 5797–5803, Aug. 2008, doi: 10.1007/s10853-008-2867-8.

[27] N. M. Rusin and A. L. Skorentsev, "Influence of the Sliding Velocity on the Wear Intensity of the Sintered Hybrid Composite (Al–12Si)–40Sn upon Dry Friction," *Physics of Metals and Metallography*, vol. 121, no. 7, pp. 694–700, Jul. 2020, doi: 10.1134/S0031918X2007008X.

[28] H. Fereidouni, S. Akbarzadeh, and M. M. Khonsari, "The Relation Between Subsurface Stresses and Useful Wear Life in Sliding Contacts," *Tribology Letters,* vol. 68, no. 1, Dec. 2019, doi: 10.1007/s11249-019-1246-8.

[29] Y. J. Fan, Z. K. Li, T. Han, and W. Da Wang, "Finite Element Simulation of Abrasive Wear and Study of Wear Resistance of Material," *Advanced Materials Research,* vol. 765–767, pp. 3192–3195,Sep.2013,doi:10.4028/www.scientific.net/AMR.765- 767.3192.

[30] M. Abdi, A. K. Taheri, and A. Bakhtiarydavijani, "A new analysis method of the dry sliding wear process based on the low cycle fatigue theory and the finite element method," *Journal of Materials Engineering and Performance*, vol. 23, no. 3, pp. 1096–1106, Dec. 2013, doi: 10.1007/s11665-013-0822-6.

[31] N. Radhika and R. Subramaniam, "Wear behaviour of aluminium/alumina/graphite hybrid metal matrix composites using Taguchi's techniques," *Industrial Lubrication and Tribology*, vol. 65, no. 3, pp. 166–174, Apr. 2013, doi: 10.1108/00368791311311169.

[32] N. Radhika and R. Raghu, "Three body abrasion wear behaviour of functionally graded aluminium/B4C metal matrix composite using design of experiments," in *Procedia Engineering*, vol. 97, pp. 713–722, Jan. 2014, doi: 10.1016/j.proeng.2014.12.301.